

# Geophysical Research Letters



## RESEARCH LETTER

10.1029/2019GL084309

### Key Points:

- A symmetric instability event is observed in a quiescent mid-ocean region
- Symmetric instability is associated with elevated upper-ocean kinetic energy, restratification, and turbulent dissipation
- The event is triggered by wind forcing of a transient front generated by mesoscale frontogenesis

### Supporting Information:

- Supporting Information S1

### Correspondence to:

X. Yu,  
xiaolong.yu@ifremer.fr

### Citation:

Yu, X., Naveira Garabato, A. C., Martin, A. P., Evans, D. G., & Su, Z. (2019). Wind-forced symmetric instability at a transient mid-ocean front. *Geophysical Research Letters*, 46, 11,281–11,291. <https://doi.org/10.1029/2019GL084309>

Received 27 JUN 2019

Accepted 5 SEP 2019

Accepted article online 12 SEP 2019

Published online 19 OCT 2019

## Wind-Forced Symmetric Instability at a Transient Mid-Ocean Front

Xiaolong Yu<sup>1</sup> , Alberto C. Naveira Garabato<sup>2</sup> , Adrian P. Martin<sup>3</sup> , D. Gwyn Evans<sup>2</sup> , and Zhan Su<sup>4</sup>

<sup>1</sup>Ifremer, Univ. Brest, CNRS, IRD, Laboratoire d'Océanographie Physique et Spatiale (LOPS), IUEM, Brest, France, <sup>2</sup>Ocean and Earth Science, University of Southampton, Southampton, UK, <sup>3</sup>National Oceanography Centre, Southampton, UK, <sup>4</sup>Massachusetts Institute of Technology, Cambridge, MA, USA

**Abstract** Mooring and glider observations and a high-resolution satellite sea surface temperature image reveal features of a transient submesoscale front in a typical mid-ocean region of the Northeast Atlantic. Analysis of the observations suggests that the front is forced by downfront winds and undergoes symmetric instability, resulting in elevated upper-ocean kinetic energy, restratification, and turbulent dissipation. The instability is triggered as downfront winds act on weak upper-ocean vertical stratification and strong lateral stratification produced by mesoscale frontogenesis. The instability's estimated rate of kinetic energy extraction from the front accounts for the difference between the measured rate of turbulent dissipation and the predicted contribution from one-dimensional scalings of buoyancy- and wind-driven turbulence, indicating that the instability underpins the enhanced dissipation. These results provide direct evidence of the occurrence of symmetric instability in a quiescent open-ocean environment and highlight the need to represent the instability's restratification and dissipative effects in climate-scale ocean models.

**Plain Language Summary** Oceanic submesoscale flows, with typical spatial scales of 1 km, are key to providing a dynamical route from energetic mesoscale eddies (10–100 km) to turbulent microscales (~1 cm). A submesoscale phenomenon thought to draw kinetic energy from mesoscale currents and transfer it to turbulent dissipative processes is symmetric instability. This mechanism has been abundantly documented in strong and persistent ocean fronts such as those associated with western boundary currents, but its occurrence and impacts in the more extensive, quiescent mid-ocean regions remain little explored. In this work, we present rare observational evidence of symmetric instability at a transient front in a mid-ocean area of the Northeast Atlantic, founded on high-resolution mooring and glider measurements. We show that wind-driven frictional effects at the front trigger a symmetric instability, which leads to elevated upper-ocean kinetic energy, restratification, and turbulent dissipation. The instability's extraction of kinetic energy from the front quantitatively matches the measured dissipation, which cannot be explained by classical one-dimensional mixed layer processes. Our findings suggest that submesoscale symmetric instability may occur extensively in the relatively quiescent environment that characterizes the majority of the ocean and point to the need of representing the instability's effects in climate-scale ocean models.

## 1. Introduction

The ocean surface boundary layer controls exchanges of tracers such as heat, momentum, and carbon between the atmosphere and the ocean interior and thus plays an important role in global tracer budgets and Earth's climate. Classical theories for the evolution of the ocean surface boundary layer and its underpinning mechanisms are generally governed by surface processes (e.g., wind stress and air-sea buoyancy flux), and the turbulence generated by these processes is typically parameterized as being one-dimensional in the vertical in climate-scale ocean models, such as in the K-profile parameterization (Large et al., 1994). Three-dimensional ocean fronts characterized by elevated lateral buoyancy gradients, however, are ubiquitous and dynamically important features of the ocean surface boundary layer (e.g., Ferrari, 2011; Tandon & Garrett, 1994; Torres et al., 2018). In recent years, observational and modeling studies have increasingly shown that submesoscale fronts, with spatial scales of O(0.1–10) km and time scales of O(1) day, may play a key role in determining the depth of the ocean surface boundary layer, turbulent mixing in the upper ocean, and the vertical transport of tracers across the mixed layer base (D'asaro et al., 2011; Klein et al., 2019; Lévy et al., 2018; Sasaki et al., 2014; Su et al., 2018).

©2019. The Authors.

This is an open access article under the terms of the Creative Commons Attribution License, which permits use, distribution and reproduction in any medium, provided the original work is properly cited.

A common outcome in the development of an ocean front is the occurrence of instabilities. At the submesoscale, a variety of overturning instabilities may occur when the Ertel potential vorticity  $q$  acquires the opposite sign to the local Coriolis parameter  $f$  (i.e.,  $fq < 0$ ; Hoskins, 1974). These instabilities include gravitational instability (GI), symmetric instability (SI), and centrifugal instability (CI). SI is the focus of this paper. SI grows by extracting kinetic energy from the vertical shear of the background flow, with perturbations independent of the along-front direction (Stone, 1966). An ocean flow may develop SI when the instability criterion  $fq < 0$  is met as a result of the flow's strong vertical shear and lateral buoyancy gradients (Thomas et al., 2013). Thus, the occurrence of SI fundamentally relies on the formation of sharp fronts to generate a layer of low potential vorticity. According to the impermeability theorem (Haynes & McIntyre, 1987), destabilizing atmospheric forcing is required to generate upper-ocean SI in a rotating stable flow (Hoskins, 1974). Specifically, surface winds aligned with the geostrophic shear (i.e., downfront winds) can induce an Ekman transport that moves dense water toward the light side of a front (Thomas, 2005). This process reduces the stratification of a surface layer and thereby provides the necessary conditions for SI.

In the presence of a strong lateral buoyancy gradient, classical turbulent convection (i.e., upright convection) in the ocean may be modulated by thermal wind shear so that the overturning circulations associated with SI occur along isopycnals that are slanted to the vertical (i.e., slantwise convection; Haine & Marshall, 1998). Taylor and Ferrari (2010) demonstrate that the ocean mixed layer may be characterized by a near-surface convective layer and a forced-SI layer beneath. In the near-surface convective layer, available potential energy is the dominant energy source for overturning motions, convective mixing develops, and the water column remains unstable. In the forced-SI layer, the dominant energy source stems instead from the background vertical shear, slanted overturning motions linked to SI dominate over convective mixing, and the water column is restratified.

Previous observational studies show that SI in the upper ocean may provide an effective exchange pathway between the mixed layer and pycnocline and play a significant role in the ocean circulation's energy balance. While these investigations were mostly conducted in regions with strong, persistent fronts and surface forcing, such as the Gulf Stream (Thomas et al., 2013; 2016), the Kuroshio (D'asaro et al., 2011), and the Antarctic Circumpolar Current (Adams et al., 2017; Viglione et al., 2018), a growing body of work from numerical models (e.g., Brannigan, 2016; Skyllingstad et al., 2017) and, more indirectly, from observations (e.g., du Plessis et al., 2019; Thompson et al., 2016) suggests that SI may also be important in more quiescent open-ocean environments, which extend across the bulk of the global ocean. However, direct and definitive evidence has been lacking. Observing signatures of SI in the open ocean is especially challenging, because fronts are often ephemeral, and surface forcing intermittent in direction and strength.

In this study, we provide observational evidence of forced SI at a transient mid-ocean front. These diagnostics are based on upper-ocean measurements obtained from a submesoscale-resolving mooring and glider array, deployed in the Northeast Atlantic as part of the U.K. OSMOSIS (Ocean Surface Mixing, Ocean Submesoscale Interaction Study) experiment. We show that the front, which is generated by mesoscale frontogenesis, undergoes SI as downfront wind-driven Ekman currents erode upper-ocean stratification. The instability's development results in elevated upper-ocean kinetic energy, restratification, and turbulent dissipation, as expected from theoretical descriptions of SI. The paper is organized as follows. The OSMOSIS data set and our methodology are introduced in section 2, and the transient submesoscale front is documented in section 3. Section 4 presents observational evidence of the occurrence of SI. Conclusions are given in section 5.

## 2. Data and Methods

### 2.1. Data

*Mooring observations.* As part of the OSMOSIS project, nine subsurface moorings were deployed over the Porcupine Abyssal Plain (48.63–48.75° N, 16.09–16.27° W; Figure 1a) in the Northeast Atlantic Ocean for the period September 2012 to September 2013 (Buckingham et al., 2016; Yu et al., 2019). The mooring array was arranged in two concentric quadrilaterals with side lengths of ~13 km (outer cluster) and ~2 km (inner cluster) around a centrally located single mooring (Figure S1a in the supporting information). This configuration enabled simultaneous measurements of mesoscale and submesoscale properties. Mooring sensors comprised a series of paired MicroCAT conductivity-temperature-depth

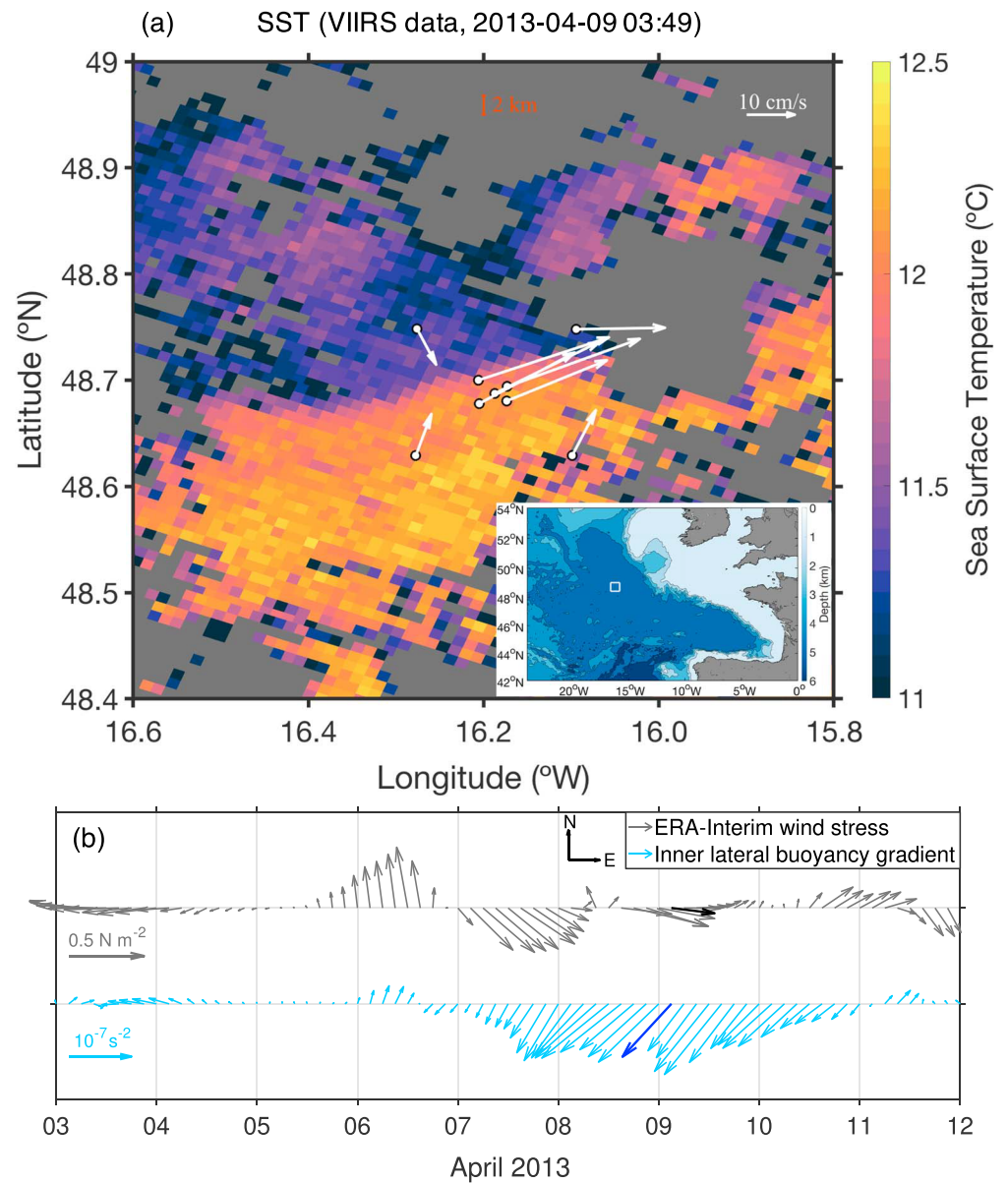


**Figure 1.** (a) Visible and Infrared Imaging Radiometer Suite (VIIRS) sea surface temperature (SST) in the Ocean Surface Mixing, Ocean Submesoscale Interaction Study region on 9 April 2013 at 03:49 UTC. Ocean Surface Mixing, Ocean Submesoscale Interaction Study moorings are shown as white dots. Data missing due to cloud cover are colored in gray. White vectors denote horizontal currents measured at a depth of 50 m by current meters on the nine moorings on 9 April 2013 at 03:50 UTC. A 2-km-distance scale is shown in light red for reference. The location of the VIIRS image is marked as a white box in the inset. (b) Time series of ERA-interim wind stress and inner lateral buoyancy gradient vectors from 3 to 12 April 2013. Vectors at 03:00 UTC on 9 April 2013 are shown in bold. Arrows indicate direction.

sensors and acoustic current meters at different depths, spanning the approximate depth interval 30–530 m. Temperature, salinity, and horizontal velocity measured at current meter and conductivity-temperature-depth instruments from the nine moorings were interpolated onto a uniform depth grid (10-m intervals between depths of 50 and 520 m) and averaged onto hourly intervals. Further, a fourth-order low-pass Butterworth filter with a cutoff of one inertial period (16 hr) was then applied to the hourly data to remove superinertial motions. In this study, we use the mooring data collected from 3 to 12 April 2013, focusing on a particular submesoscale frontal event. More details on the OSMOSIS moorings, including observational uncertainties, are provided in Yu et al. (2019).

*Seaglider observations.* In addition to the mooring observations, the OSMOSIS region (approximately  $20 \times 20$  km) was continuously sampled by at least two (five in total) autonomous underwater gliders for the entire year (Damerell et al., 2016; Erickson & Thompson, 2018; Evans et al., 2018; Thompson et al., 2016). The gliders navigated in a bow tie pattern across the mooring array, measuring temperature and salinity profiles within the top 1,000 m of the ocean at approximately 1-m depth intervals. Thompson et al. (2016) offer a comprehensive characterization of the conditions for submesoscale instabilities under the framework of potential vorticity from the yearlong glider data, with a focus on the instabilities' impact on upper-ocean stratification. Here, we additionally consider the glider-derived dissipation rate (Evans et al., 2018). As with the mooring data, this study focuses on a subset of glider observations from 3 to 12 April 2013 (Figure S1).

*Satellite observations.* Thermal imagery from the Visible and Infrared Imaging Radiometer Suite (VIIRS) is employed for the operational sea surface temperature (SST) product, owing to its high spatial resolution (750 m) under cloud-free conditions (Schloesser et al., 2016). As indicated by Buckingham et al. (2017), our study domain is commonly cloud-free every few weeks. During 3–12 April 2013, one informative VIIRS SST image could be obtained (Figure 1a).

*Reanalysis data sets.* Air-sea heat and freshwater fluxes and wind stress data are taken from the ECMWF (European Centre for Medium-Range Weather Forecasting) ERA-Interim reanalysis product with a time interval of 3 hr (Dee et al., 2011). Using fields with a horizontal resolution of  $0.75^\circ$ , data are linearly interpolated onto the OSMOSIS central mooring site. The net heat flux is calculated as the sum of shortwave radiation, longwave radiation, latent heat flux, and sensible heat flux. The reanalysis winds were validated with observed wind data from a neighboring Met Office buoy (at  $48.701^\circ$  N,  $12.401^\circ$  W), which is available from 5 September to 28 December 2012 (Yu, 2018). The ECMWF reanalysis and observed winds exhibit a good agreement, with a correlation coefficient of 0.74, and mean squared coherence  $>0.8$  for subinertial time scales.

## 2.2. Surface Forcing

Convection in the mixed layer is driven by a surface buoyancy flux, given by

$$B_0 = g\alpha Q_{net}/\rho_0 c_p + g\beta S(E-P), \quad (1)$$

where  $g$  is the acceleration due to gravity;  $\rho_0 = 1,025 \text{ kg/m}^3$  is a reference density;  $c_p$  is the specific heat capacity of seawater;  $S$  is the surface salinity;  $\alpha$  and  $\beta$  are the thermal expansion and haline contraction coefficients, respectively; and  $Q_{net}$  and  $(E-P)$  are the ECMWF net heat and freshwater fluxes, respectively.

Following Thomas and Taylor (2010), wind forcing of fronts can induce an Ekman buoyancy flux, expressed as

$$B_e = -\vec{k} \cdot (\vec{\tau} \times \nabla_h b) / \rho_0 f, \quad (2)$$

where  $\vec{k}$  is a unit vector in the vertical;  $\vec{\tau}$  is the wind stress vector;  $\nabla_h b = (\partial b/\partial x, \partial b/\partial y)$  is the horizontal buoyancy gradient, with  $b = -g(\rho - \rho_0)/\rho_0$  as the buoyancy and  $\rho$  as the potential density referenced to the surface; and  $f = 1.1 \times 10^{-4} \text{ s}^{-1}$  is the local Coriolis frequency. Note that positive values of  $B_0$  and  $B_e$  indicate destabilizing forcing.

The Ekman buoyancy flux can also be represented in terms of an equivalent heat flux, defined as  $Q_e = \frac{\rho_0 c_p}{g\alpha} B_e$ . Similarly, the equivalent surface heat flux is defined as  $Q_0 = \frac{\rho_0 c_p}{g\alpha} B_0$ .

## 2.3. Convective Layer Depth ( $h$ )

Following Bachman et al. (2017), a quartic equation is used to solve for the convective layer depth  $h$ ,

$$\left(\frac{h}{H}\right)^4 - c^3 \left(1 - \frac{h}{H}\right)^3 \left[ \frac{w_*^3}{|\Delta u_g|^3} + \frac{u_*^2}{|\Delta u_g|^2} \cos \theta_w \right]^2 = 0, \quad (3)$$

where  $w_* = (B_0 H)^{1/3}$  is the convective velocity,  $u_* = \sqrt{|\tau|/\rho_0}$  is the frictional velocity,  $u_g$  is the geostrophic velocity,  $\theta_w$  is the angle between the wind vector and the geostrophic shear, and  $c = 14$  is an empirical constant. Here we adopt the mixed layer depth  $H$  as an approximation to the surface boundary layer depth, in order to be consistent with classical scalings for dissipation associated with one-dimensional processes

(section 2.5). The mixed layer depth  $H$  is calculated from the glider data using a threshold value of density increase ( $\Delta\rho = 0.03 \text{ kg/m}^3$ ) from a near-surface value at 10 m (Damerell et al., 2016). The change in geostrophic velocity across the mixed layer,  $\Delta u_g$ , is computed by assuming geostrophic balance as  $\Delta u_g = |\partial u_g / \partial z| H = |\nabla_h b| H / f$ . Note that the convective layer depth  $h$  solved for here is always no greater than the mixed layer depth  $H$ .

#### 2.4. Categorizing Instability Types

To identify the potential submesoscale instability types, the balanced Richardson number angle  $\phi_{Ri_b} = \tan^{-1}(-f^2 N^2 / |\nabla_h b|^2)$  and the critical angle  $\phi_C = \tan^{-1}(-\zeta / f)$  are computed following Thomas et al. (2013), with  $N^2 = \partial b / \partial z$  as the vertical stratification and  $\zeta = f + \nabla \times u_g \cdot \vec{k}$  as the vertical component of the absolute vorticity of the geostrophic flow. This approach has been used by previous studies to assess the susceptibility of the flow to submesoscale instabilities (e.g., Naveira Garabato et al., 2017; Ramachandran et al., 2018; Thompson et al., 2016; Viglione et al., 2018). The instability criterion for GI, SI, and CI may be expressed as the following:

- (i) For unstable vertical stratification (i.e.,  $N^2 < 0$ ), GI is expected to dominate when  $-180^\circ < \phi_{Ri_b} < -135^\circ$ , and a hybrid GI/SI will occur when  $-135^\circ < \phi_{Ri_b} < -90^\circ$ .
- (ii) For stable stratification (i.e.,  $N^2 > 0$ ) and cyclonic vertical vorticity, SI is predicted to develop when  $-90^\circ < \phi_{Ri_b} < \phi_C$ , with  $\phi_C < -45^\circ$ .
- (iii) For stable stratification (i.e.,  $N^2 > 0$ ) and anticyclonic vertical vorticity, SI is expected for  $-90^\circ < \phi_{Ri_b} < -45^\circ$  with  $\phi_C > -45^\circ$ , and a hybrid SI/CI is predicted when  $-45^\circ < \phi_{Ri_b} < \phi_C$ .

Note that this analysis does not take into account mixed layer baroclinic instability (which can arise when  $f\bar{q} > 0$ ) and the modification of stratification by surface waves (Hamlington et al., 2014).

#### 2.5. Calculation of Turbulent Dissipation Rate

The rate of dissipation of turbulent kinetic energy  $\epsilon_{obs}$  is estimated from high-frequency fluctuations in the glider vertical velocity using a generalization of the large eddy method of Beaird et al. (2012) developed by Evans et al. (2018) and used here to explore the key contributions to dissipation at the transient front. A filter with a cutoff dependent on the local buoyancy frequency is applied to glider vertical velocity estimates to remove internal wave variability. The glider-derived dissipation rate has been compared with a yearlong time series of dissipation calculated from a 600-kHz acoustic Doppler current profiler mounted at 50 m on the central mooring and found to generally agree within confidence intervals (90% level; see Figure 1 in Evans et al., 2018).

Estimates of the depth-integrated dissipation rate in the mixed layer by one-dimensional processes associated with surface buoyancy flux ( $\overline{\epsilon}_0$ ) and wind-driven turbulence ( $\overline{\epsilon}_\tau$ ) are provided by  $\overline{\epsilon}_0 = B_0 H / 2$  and  $\overline{\epsilon}_\tau = \int_{-H}^0 \frac{u_z^2}{\kappa z} dz$ , respectively, where  $\kappa = 0.4$  is the von Karman constant and the overline denotes an integral over the mixed layer. Following Thomas and Taylor (2010), the mixed-layer-integrated dissipation rate associated with the Ekman buoyancy flux can be computed as  $\overline{\epsilon}_e = B_e H / 2$ .

### 3. The Submesoscale Frontal Event

A high-resolution VIIRS SST image reveals structures of a submesoscale thermal front in the OSMOSIS region on 9 April 2013 at 03:49 UTC (Figure 1a). The SST image shows a change of approximately  $1^\circ \text{ C}$  over  $O(1) \text{ km}$  at the edge of the thermal front. The horizontal velocity vectors measured at 50-m depth on the central and four inner moorings are strongly eastward with speeds exceeding  $30 \text{ cm/s}$  (bearing  $73\text{--}76^\circ$  east of north), aligned with the thermal front. A horizontally confluent flow field is indicated by the measurements from the outer moorings, suggesting a frontogenetic scenario (Hoskins, 1982). Further, geostrophic sea surface velocity and sea level anomaly from the  $0.25^\circ$  gridded altimetric product from Archiving, Validation, and Interpretation of Satellite Oceanographic data reveal that the OSMOSIS site laid in between two cyclonic mesoscale eddies at this time (Figure S2a), consistent with the thermal front having been generated by the confluent flow between the eddies. This indicates that the front is a transient feature of the regional oceanic environment.

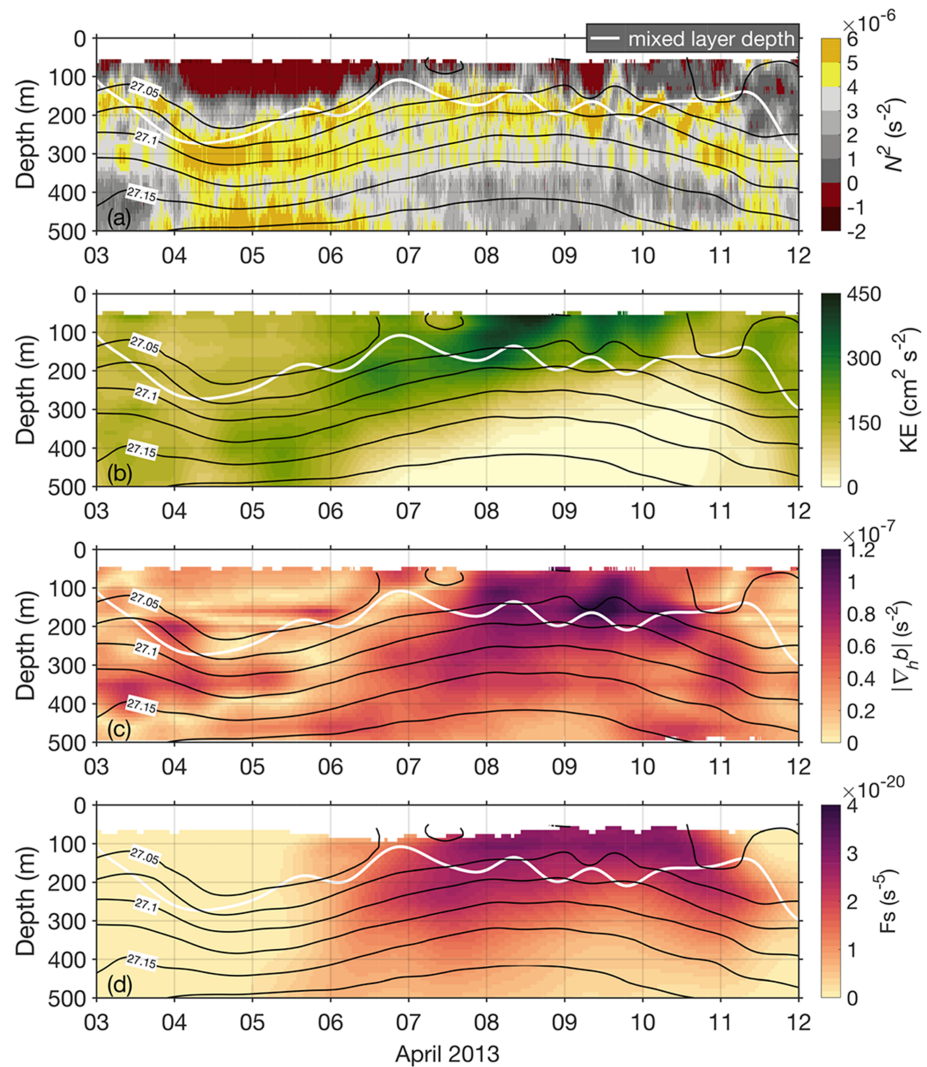


**Figure 2.** Time series of subinertial (a) vertical buoyancy stratification, (b) kinetic energy, (c) submesoscale lateral buoyancy gradient *inner*  $|\nabla_h b|$ , and (d) mesoscale frontogenesis function *outer*  $F_s$ , at the central mooring site from 3 to 12 April 2013. The white line indicates the mixed layer depth. Isopycnals are overlaid as black contours at intervals of  $0.025 \text{ kg/m}^3$  in (a–d), ranging from  $27.05$  to  $27.175 \text{ kg/m}^3$ .

The lateral buoyancy gradient estimated from the inner mooring cluster (hereinafter *inner*  $\nabla_h b$ ) prior to and after the frontal event (7–11 April) was weak and variable in magnitude and direction (Figure 1b). By contrast, *inner*  $\nabla_h b$  steadily increased on 7 April, directed southwestward, and remained large with a magnitude of order  $10^{-7} \text{ s}^{-2}$  during 8–10 April, after which *inner*  $\nabla_h b$  gradually weakened. Compared to *inner*  $\nabla_h b$ , wind stress forcing  $\vec{\tau}$  was more variable throughout our study period (3–12 April). Nonetheless, a significant downfront component aligned with the frontal flow (i.e., perpendicular to *inner*  $\nabla_h b$ ) was observed at various times during the frontal event, lasting for several hours each time (e.g., see blue and black arrows on 9 April in Figure 1b). The downfront component of the wind stress attained a maximum value in excess of  $0.25 \text{ N/m}^2$  during the study period, approximately a factor of 3 larger than the annual-mean wind stress of  $0.09 \text{ N/m}^2$ .

Prior to the frontal event (7 April), a gravitationally unstable layer (i.e.,  $N^2 < 0$ ) was observed above a depth of 150 m, with the deepest mixed layer extending down to about 300 m (Figure 2a). The mixed layer base abruptly shoaled to approximately 100 m on 6–7 April, after which the mixed layer depth fluctuated within the range of 100 to 200 m. The mixed layer was often weakly stratified, with a characteristic  $N^2 \sim 1 \times 10^{-6} \text{ s}^{-2}$  (seen in Figure 2a as dark gray) that was 1 order of magnitude smaller than mixed-layer values of  $N^2 \sim 1 \times 10^{-5} \text{ s}^{-2}$  documented in winter in the midlatitude Southern Ocean (du Plessis et al., 2019).

The kinetic energy, defined as  $KE = (u^2 + v^2)/2$  (where  $u$  and  $v$  denote the zonal and meridional velocity components, respectively), exhibits a clear signature of mixed-layer-intensified frontal flows on 7–11 April, indicating enhanced vertical shear (Figure 2b). Consistent with this, the mixed layer is characterized by increased *inner*  $|\nabla_h b|$  during the same period (Figure 2c), despite strong density compensation between temperature and salinity gradients (Figures S1b–S1c). Assessment of the degree of geostrophy from the inner mooring cluster shows that submesoscale subinertial flows are largely in geostrophic balance (Yu et al., 2019). *inner*  $|\nabla_h b|$  frequently exceeds  $1 \times 10^{-7} \text{ s}^{-2}$ , approximately a factor of 4 larger than the annual-mean *inner*  $|\nabla_h b|$  of  $2.6 \times 10^{-8} \text{ s}^{-2}$ .

Instances of elevated *inner*  $|\nabla_h b|$  are concurrent with a period of mesoscale frontogenesis, as indicated by a frontogenesis function (Figure 2d) estimated from the outer mooring cluster (hereinafter *outer* Fs). The frontogenesis function is defined as  $Fs = \vec{Q} \cdot \nabla_h b$ , where  $\vec{Q} = (-\frac{\partial u}{\partial x} \frac{\partial b}{\partial x} - \frac{\partial v}{\partial x} \frac{\partial b}{\partial y}, -\frac{\partial u}{\partial y} \frac{\partial b}{\partial x} - \frac{\partial v}{\partial y} \frac{\partial b}{\partial y})$  is the Q vector (Hoskins, 1982). High *outer* Fs denotes that the strong baroclinicity of the submesoscale front is likely to be associated with intense mesoscale frontogenesis, induced by the substantial confluent flows (Figure 1a) and elevated strain rates (Figure S2b). *outer* Fs attains a maximum of  $4 \times 10^{-20} \text{ s}^{-5}$ , 1 order of magnitude larger than the annual root mean square *outer* Fs of  $\sim 2 \times 10^{-21} \text{ s}^{-5}$ . Values of *outer* Fs exceeding  $10^{-20} \text{ s}^{-5}$  occur about 4.3% of the entire year. Notably, the vertical extent of the enhancement of *inner*  $|\nabla_h b|$  and *outer* Fs exceeds that of the mixed layer, although the enhancement's amplitude decreases gently with depth.

Enhanced values of the upward vertical buoyancy flux (i.e., the rate of restratification by the vertical flow) with a root mean square of order  $O(10^{-7}) \text{ m}^2/\text{s}^3$  extend down to at least 200 m below the mixed layer base (Figure S3). The vertical buoyancy flux is more surface intensified and attains an overall mean value of  $5 \times 10^{-8} \text{ m}^2/\text{s}^3$  during the frontal event, equivalent to a restratifying heat flux of  $69 \text{ W/m}^2$ . This restratifying action is most likely a consequence of mesoscale-strain-induced frontogenesis (Yu et al., 2019), which drives a thermally direct secondary circulation and corresponds to a transformation of available potential energy into kinetic energy (McWilliams, 2016). This process may precondition the flow to become unstable to SI, as evidenced by the concurrence of the SI event discussed in the present paper and the upward buoyancy flux.

Overall, conditions in the mixed layer were favorable to the development of SI during the frontal event (7–11 April). These conditions included a strong horizontal buoyancy gradient (*inner*  $|\nabla_h b| \sim 10^{-7} \text{ s}^{-2}$ ) and reduced static stability ( $N^2 \sim 10^{-6} \text{ s}^{-2}$ ). Further, the ratio of the square of the lateral buoyancy gradient to the vertical stratification, which defines the balanced Richardson number  $Ri_b = f^2 N^2 / |\nabla_h b|^2$ , was close to 1, a prerequisite for the occurrence of active submesoscale motions (Thomas et al., 2008). According to the linear stability analysis (Stone, 1966), the fastest-growing mode of SI during the frontal event has a linear inverse growth rate of a few hours, and the associated wavelength ranges from 1 to 5 km. In the next section, we look for direct evidence that SI is the key process underpinning the intensification of submesoscale flows during the study period.

#### 4. Observational Evidence of SI

The first step in assessing the potential occurrence of SI is to quantify the external forcing responsible for the modification of the flow's potential vorticity. For the upper ocean, destabilizing atmospheric forcing (i.e.,  $B_0 + B_e > 0$ ) is a necessary condition for the development of SI (Thomas & Taylor, 2010). Figure 3a shows that the Ekman buoyancy flux, driven by persistent downfront winds, dominated over the surface buoyancy flux in terms of equivalent heat flux during the frontal event. The Ekman buoyancy flux reached a peak equivalent to  $650 \text{ W/m}^2$  of oceanic heat loss on 8 April, which was larger than the surface buoyancy flux by a factor of 6. The surface forcing at the OSMOSIS site was dominated by atmospheric cooling prior to the frontal event, between 4 and 7 April, and this resulted in deepening of the mixed layer down to 300 m via GI (Figure 2a). Subsequently, the equivalent surface heat flux steadily decreased from its maximum of  $200 \text{ W/m}^2$  to less than  $100 \text{ W/m}^2$  on 7 April (not shown). This stage of surface cooling may have played a role in preconditioning vertical stratification for the occurrence of SI.

Second, following Thomas et al. (2013), we use  $\phi_{Ri_b}$  to classify instabilities within the inner mooring cluster (see section 2.4). Figure 3b shows that SI conditions prevailed on 8–11 April and that they preferentially

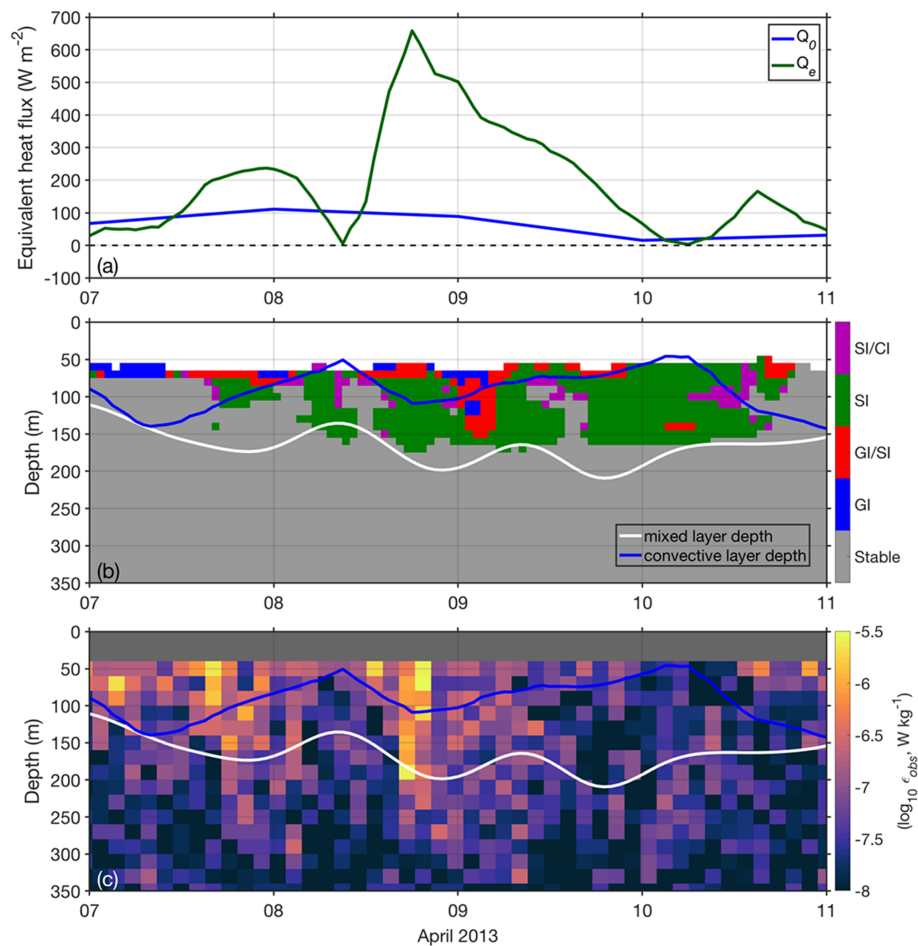


**Figure 3.** Time series of (a) equivalent surface heat flux (blue) and Ekman buoyancy flux (dark green) expressed in units of heat flux, (b) subsurface instability categories, and (c) glider-based dissipation rate during the frontal event. Positive values in (a) indicate conditions favorable for forced symmetric instability. The white and blue lines in (b) and (c) indicate the mixed layer depth and convective layer depth, respectively.

occurred below the convective layer (green shading between blue and white contours in Figure 3b). This is consistent with theoretical descriptions of slantwise convection (Taylor & Ferrari, 2010).

Third, the glider-derived dissipation is frequently elevated during the frontal event, with values on the order of  $10^{-6}$  W/kg (3 orders of magnitude above ocean background values of  $10^{-9}$  W/kg) in the mixed layer (Figure 3c). The peak of turbulent dissipation during 8–9 April matches well with the maximum in the Ekman buoyancy flux (Figure 3a), suggesting a causal link between the downfront wind forcing and the observed energy dissipation. The elevated dissipation extends throughout the mixed layer, consistent with the vertical extent of the SI diagnosed in Figure 3b.

To quantitatively link the observed elevated dissipation rates with the SI-favorable conditions during our study period, we compare the glider-derived dissipation rate to those predicted to be driven by SI and by one-dimensional processes associated with surface air-sea buoyancy fluxes and wind forcing (Figures 4a and 4b). We conservatively disregard the glider-derived dissipation at depths less than 50 m, in order to exclude surface wave effects (Gargett, 1989). The mixed layer dissipation accounted for by one-dimensional processes (black curve in Figure 4b) exhibits a deficit of a factor of 2 to 3 when compared with the glider-derived dissipation (magenta curve in Figure 4b). This deficit is most evident on 8–9 April, when the Ekman buoyancy flux peaked and conditions were conducive to SI. By contrast, a strong agreement with the glider-derived dissipation can be seen for the combined one-dimensional processes and SI, especially on 8–9 April. This indicates that the difference between the glider-derived dissipation and the contribution of one-dimensional processes can be explained by subsurface SI forced by downfront winds.

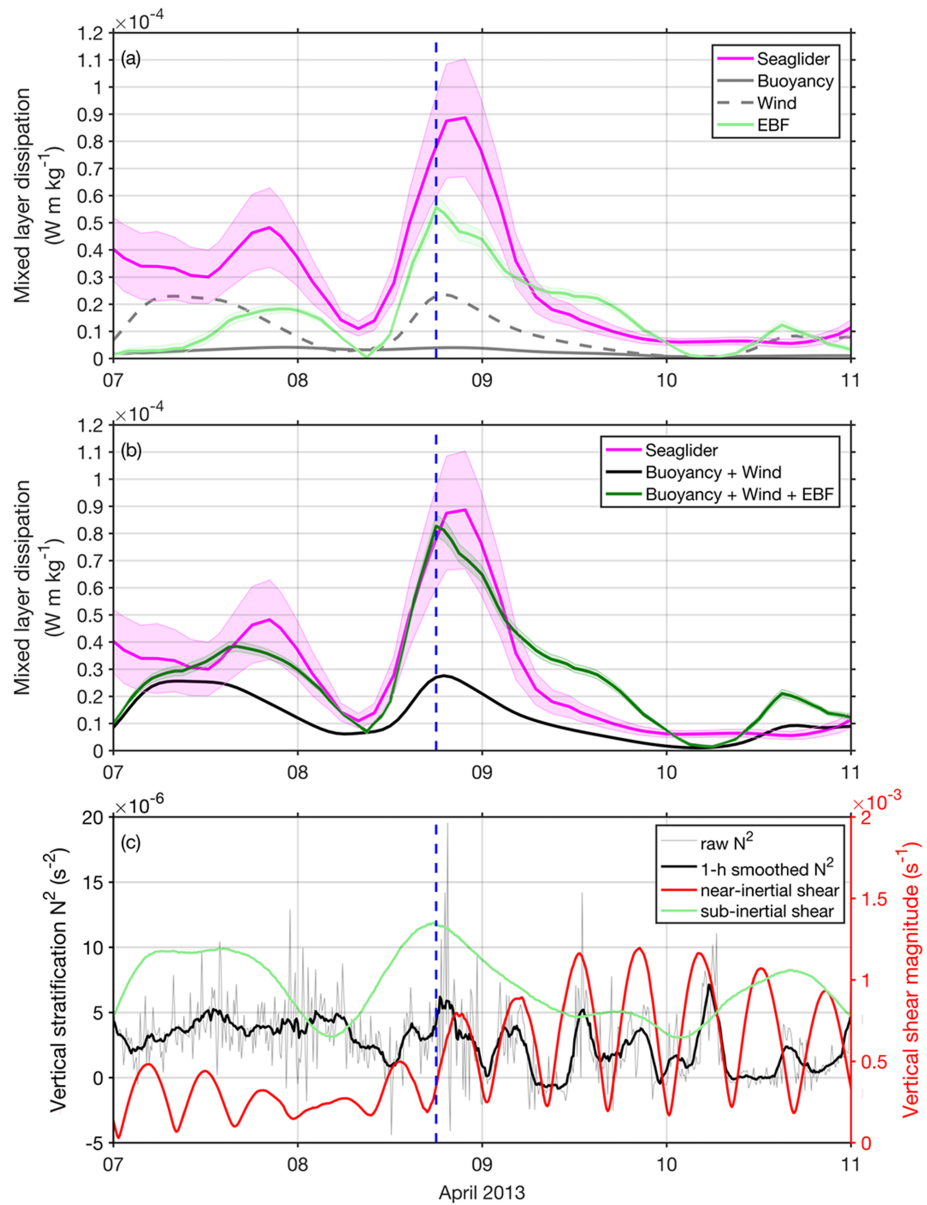


**Figure 4.** (a) Time series of mixed-layer-integrated (from the mixed layer base to a depth of 50 m) dissipation estimated from the glider observations ( $\overline{\epsilon}_{obs}$ , magenta), surface buoyancy ( $\overline{\epsilon}_0$ , solid dark gray), surface wind stress ( $\overline{\epsilon}_\tau$ , dashed dark gray), and Ekman buoyancy flux (EBF;  $\overline{\epsilon}_\tau$ , light green). (b) Time series of mixed-layer-integrated dissipation estimated from the glider observations  $\overline{\epsilon}_{obs}$  (magenta),  $\overline{\epsilon}_0 + \overline{\epsilon}_\tau$  (black), and  $\overline{\epsilon}_0 + \overline{\epsilon}_\tau + \overline{\epsilon}_\tau$  (green). The shaded regions illustrate the 90% confidence envelope of the integrated dissipation estimated by a Monte Carlo approach. (c) Time series of raw (gray) and 1-hr smoothed (black) vertical stratification (left axis), and the magnitude of near-inertial (red) and subinertial (light green) vertical shears (right axis) at 150-m depth. The vertical dashed blue lines correspond to the time when the EBF is largest. Near-inertial motions are defined as the velocity in the frequency band of  $(0.8, 1.2)f$ .

A final point of note is that, during the SI event, sheared inertial oscillations were also excited by surface winds (Figure S4). Inertial shear was greatly enhanced in the close proximity of the mixed layer base and substantially modulated vertical stratification via phase-dependent horizontal advection (especially on 9–10 April; Figure 4c). This observation agrees with the idealized simulations of Thomas et al. (2016). While the temporal variability of stratification may have been important in the evolution of SI (e.g., by modifying the Richardson number), the magnitude of the inertial shear in the downfront direction was found to be considerably smaller than that of the subinertial shear (Figure S4c). This confirms that subinertial shear was most likely the primary factor determining turbulent dissipation during our observed SI event.

## 5. Conclusions

The OSMOSIS mooring and glider measurements provide a unique observational data set that enables a dynamical description of upper-ocean forced submesoscale instabilities with horizontal scales down to O (1 km). In this work, we conduct a case study of a SI event in this mid-ocean setting, based on four lines of direct observational evidence: (i) Upper-ocean kinetic energy is enhanced during the SI event (Figure 2b), as expected from the active development of a submesoscale instability; (ii) the event is associated with downfront winds and mesoscale frontogenesis (Figures 1b and 2d), conditions that favor the onset of SI and that are regularly met in mid-ocean environments; (iii) a shoaling of the mixed layer is observed (Figure 2a), consistent with theoretical predictions for SI; and (iv) dissipation is elevated in a manner quantitatively consistent with SI extracting kinetic energy from the background flow, which is broadly in geostrophic balance (Figure 4).

Our work indicates that the SI event is likely to have been triggered by downfront winds, as air-sea heat fluxes were generally modest, consistent with previous observations (e.g., Thomas et al., 2013). The OSMOSIS site lies at the eastern edge of the North Atlantic subtropical gyre, a region of weak mean flow and moderate eddy kinetic energy that is arguably representative of a substantial fraction of the global ocean. While one-dimensional turbulent processes associated with air-sea buoyancy and wind forcing are found to be the dominant driver of upper-ocean turbulent dissipation over an annual cycle (Evans et al., 2018), our case study demonstrates that SI can play an important role in sustaining dissipation at depths beyond the influence of surface waves. Further, our work suggests that SI may be a common feature throughout the quiescent regions of the ocean, where it can be induced by the occasional alignment of surface winds with transient upper-ocean fronts generated by mesoscale frontogenesis. Assessment of the relative importance of forced SI and surface-forced processes (including the effects of surface waves) to total turbulent dissipation in the ocean surface boundary layer is the subject of a separate study, led by C. E. Buckingham.

### Acknowledgments

We are grateful to the officers, crew, scientists, and technicians of the RRS *Discovery*, RRS *James Cook*, and R/V *Celtic Explorer*, for their hard work in deploying and recovering the OSMOSIS moorings and gliders. All data are archived at the British Oceanographic Data Centre (glider data are accessible at <https://doi.org/10/cq6>). This work was funded by grants from the Natural Environmental Research Council (NE/1019999/1, NE/1019905/1, and NE/1020083/1) and the National Science Foundation (NSF-OCE 1155676) as part of the OSMOSIS project. We thank Christian E. Buckingham and Zammath Khaleel for processing and making available the yearlong VIIRS SST data for the OSMOSIS region. We are thankful for the efforts of Gillian Damerell and the University of East Anglia and Caltech glider teams who collectively piloted the gliders and produced the final calibrated data set. We also thank Andrew F. Thompson for useful comments. X. Y. gratefully acknowledges the support of the ANR project 17-CE01-0006-01 and the China Scholarship Council, and A. C. N. G. that of the Royal Society and the Wolfson Foundation. Z. S. was supported by NSF award OAC-1835618 (Collaborative Research: Framework: Data: Toward Exascale Community Ocean Circulation Modeling) and NASA Grant NNX15AG42G. ERA-Interim data were obtained from the European Centre for Medium-Range Weather Forecasts (downloaded from <http://www.ecmwf.int/en/research/climate-reanalysis/era-interim>).

## References

- Adams, K. A., Hosegood, P., Taylor, J. R., Sallee, J. B., Bachman, S., Torres, R., & Stamper, M. (2017). Frontal circulation and submesoscale variability during the formation of a Southern Ocean mesoscale eddy. *Journal of Physical Oceanography*, *47*(7), 1737–1753.
- Bachman, S. D., Fox-Kemper, B., Taylor, J. R., & Thomas, L. N. (2017). Parameterization of frontal symmetric instabilities. I: Theory for resolved fronts. *Ocean Modelling*, *109*, 72–95.
- Beard, N., Fer, I., Rhines, P., & Eriksen, C. (2012). Dissipation of turbulent kinetic energy inferred from seagliders: An application to the eastern nordic seas overflows. *Journal of Physical Oceanography*, *42*(12), 2268–2282.
- Brannigan, L. (2016). Intense submesoscale upwelling in anticyclonic eddies. *Geophysical Research Letters*, *43*, 3360–3369. <https://doi.org/10.1002/2016GL067926>
- Buckingham, C. E., Garabato, A. C. N., Thompson, A. F., Brannigan, L., Lazar, A., Marshall, D. P., et al. (2016). Seasonality of submesoscale flows in the ocean surface boundary layer. *Geophysical Research Letters*, *43*, 2118–2126. <https://doi.org/10.1002/2016GL068009>
- Buckingham, C. E., Khaleel, Z., Lazar, A., Martin, A. P., Allen, J. T., Garabato, A. C. N., et al. (2017). Testing Munk's hypothesis for submesoscale eddy generation using observations in the North Atlantic. *Journal of Geophysical Research: Oceans*, *122*, 6725–6745. <https://doi.org/10.1002/2017JC012910>
- D'asaro, E., Lee, C., Rainville, L., Harcourt, R., & Thomas, L. (2011). Enhanced turbulence and energy dissipation at ocean fronts. *Science*, *332*(6027), 318–322.
- Damerell, G. M., Heywood, K. J., Thompson, A. F., Binetti, U., & Kaiser, J. (2016). The vertical structure of upper ocean variability at the Porcupine Abyssal Plain during 2012–2013. *Journal of Geophysical Research: Oceans*, *121*, 3075–3089. <https://doi.org/10.1002/2015JC011423>
- Dee, D. P., Uppala, S. M., Simmons, A. J., Berrisford, P., Poli, P., Kobayashi, S., et al. (2011). The ERA-interim reanalysis: Configuration and performance of the data assimilation system. *Quarterly Journal of the Royal Meteorological Society*, *137*(656), 553–597.
- du Plessis, M., Swart, S., Ansgore, I. J., Mahadevan, A., & Thompson, A. F. (2019). Southern Ocean seasonal restratification delayed by submesoscale wind-front interactions. *Journal of Physical Oceanography*, *49*(4), 1035–1053.
- Erickson, Z. K., & Thompson, A. F. (2018). The seasonality of physically driven export at submesoscales in the northeast Atlantic Ocean. *Global Biogeochemical Cycles*, *32*, 1144–1162. <https://doi.org/10.1029/2018GB005927>
- Evans, D. G., Lucas, N. S., Hemsley, V., Frajka-Williams, E., Garabato, A. C. N., Martin, A., et al. (2018). Annual cycle of turbulent dissipation estimated from Seagliders. *Geophysical Research Letters*, *45*, 10,560–10,569. <https://doi.org/10.1029/2018GL079966>
- Ferrari, R. (2011). A frontal challenge for climate models. *Science*, *332*(6027), 316–317.
- Gargett, A. E. (1989). Ocean turbulence. *Annual Review of Fluid Mechanics*, *21*, 419–451.
- Haine, T. W. N., & Marshall, J. (1998). Gravitational, symmetric, and baroclinic instability of the ocean mixed layer. *Journal of Physical Oceanography*, *28*(4), 634–658.
- Hamlington, P. E., Van Roekel, L. P., Fox-Kemper, B., Julien, K., & Chini, G. P. (2014). Langmuir-submesoscale interactions: Descriptive analysis of multiscale frontal spindown simulations. *Journal of Physical Oceanography*, *44*(9), 2249–2272.
- Haynes, P. H., & McIntyre, M. E. (1987). On the evolution of vorticity and potential vorticity in the presence of diabatic heating and frictional or other forces. *Journal of the Atmospheric Sciences*, *44*(5), 828–841.
- Hoskins, B. J. (1974). The role of potential vorticity in symmetric stability and instability. *Quarterly Journal of the Royal Meteorological Society*, *100*(425), 480–482.
- Hoskins, B. J. (1982). The mathematical-theory of frontogenesis. *Annual Review of Fluid Mechanics*, *14*, 131–151.

- Klein, P., Lapeyre, G., Siegelman, L., Qiu, B., Fu, L.-L., Torres, H., et al. (2019). Ocean-scale interactions from space. *Earth and Space Science*, 6, 795–817. <https://doi.org/10.1029/2018EA000492>
- Large, W. G., McWilliams, J. C., & Doney, S. C. (1994). Oceanic vertical mixing—A review and a model with a nonlocal boundary-layer parameterization. *Reviews of Geophysics*, 32, 363–403.
- Lévy, M., Franks, P. J. S., & Smith, K. S. (2018). The role of submesoscale currents in structuring marine ecosystems. *Nature Communications*, 9, 4758.
- McWilliams, J. C. (2016). Submesoscale currents in the ocean. *Proceedings of the Royal Society A: Mathematical, Physical and Engineering Sciences*, 472(2189), 20160117.
- Naveira Garabato, A. C., Forryan, A., Dutrieux, P., Brannigan, L., Biddle, L. C., Heywood, K. J., et al. (2017). Vigorous lateral export of the meltwater outflow from beneath an antarctic ice shelf. *Nature*, 542(7640), 219–222.
- Ramachandran, S., Tandon, A., Mackinnon, J., Lucas, A. J., Pinkel, R., Waterhouse, A. F., et al. (2018). Submesoscale processes at shallow salinity fronts in the bay of bengal: Observations during the winter monsoon. *Journal of Physical Oceanography*, 48(3), 479–509.
- Sasaki, H., Klein, P., Qiu, B., & Sasai, Y. (2014). Impact of oceanic-scale interactions on the seasonal modulation of ocean dynamics by the atmosphere. *Nature Communications*, 5, 5636.
- Schloesser, F., Cornillon, P., Donohue, K., Boussidi, B., & Iskin, E. (2016). Evaluation of thermosalinograph and VIIRS data for the characterization of near-surface temperature fields. *Journal of Atmospheric and Oceanic Technology*, 33(9), 1843–1858.
- Skyllingstad, E. D., Duncombe, J., & Samelson, R. M. (2017). Baroclinic frontal instabilities and turbulent mixing in the surface boundary layer. Part ii: Forced simulations. *Journal of Physical Oceanography*, 47(10), 2429–2454.
- Stone (1966). On non-geostrophic baroclinic stability. *Journal of the Atmospheric Sciences*, 23(4), 390–400.
- Su, Z., Wang, J., Klein, P., Thompson, A. F., & Menemenlis, D. (2018). Ocean submesoscales as a key component of the global heat budget. *Nature Communications*, 9(1), 775.
- Tandon, A., & Garrett, C. (1994). Mixed-layer restratification due to a horizontal density gradient. *Journal of Physical Oceanography*, 24(6), 1419–1424.
- Taylor, J. R., & Ferrari, R. (2010). Buoyancy and wind-driven convection at mixed layer density fronts. *Journal of Physical Oceanography*, 40(6), 1222–1242.
- Thomas, L. N. (2005). Destruction of potential vorticity by winds. *Journal of Physical Oceanography*, 35(12), 2457–2466.
- Thomas, L. N., Tandon, A., & Mahadevan, A. (2008). Submesoscale processes and dynamics. In *Ocean modeling in an eddying regime* (pp. 17–38). Washington, DC: American Geophysical Union.
- Thomas, L. N., & Taylor, J. R. (2010). Reduction of the usable wind-work on the general circulation by forced symmetric instability. *Geophysical Research Letters*, 37, L18606. <https://doi.org/10.1029/2010GL044680>
- Thomas, L. N., Taylor, J. R., D'Asaro, E. A., Lee, C. M., Klymak, J. M., & Shcherbina, A. (2016). Symmetric instability, inertial oscillations, and turbulence at the gulf stream front. *Journal of Physical Oceanography*, 46(1), 197–217.
- Thomas, L. N., Taylor, J. R., Ferrari, R., & Joyce, T. M. (2013). Symmetric instability in the gulf stream. *Deep Sea Research Part II: Topical Studies in Oceanography*, 91, 96–110.
- Thompson, A. F., Lazar, A., Buckingham, C., Garabato, A. C. N., Damerell, G. M., & Heywood, K. J. (2016). Open-ocean submesoscale motions: A full seasonal cycle of mixed layer instabilities from gliders. *Journal of Physical Oceanography*, 46(4), 1285–1307.
- Torres, H. S., Klein, P., Menemenlis, D., Qiu, B., Su, Z., Wang, J. B., et al. (2018). Partitioning ocean motions into balanced motions and internal gravity waves: A modeling study in anticipation of future space missions. *Journal of Geophysical Research: Oceans*, 123, 8084–8105. <https://doi.org/10.1029/2018jc014438>
- Viglione, G. A., Thompson, A. F., Flexas, M. M., Sprintall, J., & Swart, S. (2018). Abrupt transitions in submesoscale structure in southern drake passage: Glider observations and model results. *Journal of Physical Oceanography*, 48(9), 2011–2027.
- Yu, X. (2018). An annual cycle of open-ocean submesoscale dynamics in the northeast atlantic from observations (PhD Thesis), University of Southampton.
- Yu, X., Naveira Garabato, A. C., Martin, A. P., Buckingham, C. E., Brannigan, L., & Su, Z. (2019). An annual cycle of submesoscale vertical flow and restratification in the upper ocean. *Journal of Physical Oceanography*, 49(6), 1439–1461.